Geophysical Research Letters

RESEARCH LETTER
10.1029/2025GL121312

Turbulent Mixing and Dissipation Around Rough Seamounts

Tomas Chor[1,2], **Jacob Wenegrat**[1], **and Gregory L. Wagner**[3,4]

[1]Department of Atmospheric and Oceanic Science, University of Maryland, College Park, MD, USA, [2]Atdepth MRV Inc., Cambridge, MA, USA, [3]Massachusetts Institute of Technology, Cambridge, MA, USA, [4]Aeolus Labs, San Francisco, CA, USA

Key Points:

- Small-scale topographic roughness can increase dissipation in seamount wakes by up to tenfold and enhance mixing by a factor of three
- This effect is most pronounced for seamounts typical of the Southern Ocean
- Globally, this difference is estimated to account for 30% of kinetic energy dissipation by seamounts

Supporting Information:

Supporting Information may be found in the online version of this article.

Correspondence to:

T. Chor,
tchor@umd.edu

Citation:

Chor, T., Wenegrat, J., & Wagner, G. L. (2026). Turbulent mixing and dissipation around rough seamounts. *Geophysical Research Letters*, *53*, e2025GL121312. https://doi.org/10.1029/2025GL121312

Received 15 DEC 2025
Accepted 6 APR 2026

Abstract Seamounts are critical components of the global ocean energy budget, contributing significantly to turbulent dissipation through their interaction with large-scale flows. However, most previous numerical investigations used smoothed bathymetry that omits small-scale topographic variability. We use turbulence-resolving large-eddy simulations to investigate how bathymetric roughness affects seamount wake energetics. We compare flows around realistic rough seamounts against versions smoothed over varying horizontal scales, and find that dissipation and mixing rates can differ by an order of magnitude between cases. Importantly, seamounts in the parameter regimes where roughness effects are most pronounced (low slope Burger numbers) are concentrated in the Southern Ocean, coinciding with very fast flows and resulting in leading-order effects for global dissipation due to seamounts. An implication of our results is that model horizontal spacings of at least order 100 m may be necessary to capture the full energetics in most seamount wakes in the Southern Ocean.

Plain Language Summary Seamounts are underwater mountains that play an important role in mixing ocean waters, which affects how the ocean circulates and how heat and nutrients move around the globe. Until now, computer models have usually used smooth versions of seamounts, ignoring their rough, bumpy surfaces. In this study, we use advanced high-resolution simulations to show that including small-scale roughness on seamounts can greatly increase the amount of mixing and energy loss in the ocean—sometimes by as much as a factor of 10. This effect is especially strong for seamounts located in the Southern Ocean, where currents are particularly fast. Our results suggest that many current estimates may be missing a significant portion of the mixing and dissipation caused by seamounts, and that small details on the seafloor can have big impacts on the ocean's energy budget.

1. Introduction

Seamounts, underwater mountains rising from the seafloor, have emerged as critical components of the global ocean mixing system with far-reaching implications for ocean circulation and biogeochemical budgets (Mashayek et al., 2024; Munk & Wunsch, 1998). Due to their interactions with the bottom flow, they stir and mix deep waters by many processes, including lee waves (Nikurashin et al., 2014; Perfect et al., 2020b; Wright et al., 2014) and topographic wake vortices (Aravind et al., 2026; Liu et al., 2024; Nagai et al., 2021; Perfect et al., 2018, 2020a; Srinivasan et al., 2019). The ensuing dissipation and mixing are thought to exert important control on the rate and structure of the overturning circulation, likely playing an important role in the upwelling of deep waters and global energetics (Mashayek et al., 2024; Waterhouse et al., 2014).

Previous investigations using regional models have revealed the complex dynamics and mixing patterns around seamounts (Perfect et al., 2018, 2020a; Srinivasan et al., 2019, 2021). Collectively, they show that rotation and stratification play an important role in shaping the dynamics and energetics of flows around them. For example, above a critical Burger number, vortex shedding frequency varies vertically with local seamount diameter, resulting in vertically-decoupled vortices and a vertically-sheared wake (Perfect et al., 2018). This in turn drives different energetic transfers from unsheared quasigeostrophic motions (Perfect et al., 2020a). Different combinations of rotation and stratification also lead to different dynamical instabilities, which can also shape flow energetics (Srinivasan et al., 2019, 2021). Submesoscale centrifugal instabilities are often present as a particularly energetic example (Srinivasan et al., 2019), in dynamics that were also seen in observations (Nagai et al., 2021) and near coastal bathymetric shapes (Chor & Wenegrat, 2025; Gula et al., 2016). Similar conclusions were reached by Liu et al. (2024) using turbulence-resolving simulations of a conical seamount, with the caveat that the

authors saw vertical coupling, even past the critical Burger number found by Perfect et al. (2018)—an indication that geometry may play an important role. Finally, Puthan et al. (2022) used similar turbulent simulations to investigate the effect of tides, finding complex dynamics that depend strongly on both tidal phase and strength.

Common to all the aforementioned studies is the assumption of idealized, smooth seamount geometries, which has been the standard approach in both theoretical and numerical investigations of seamount-flow interactions. Even in investigations using realistic bathymetry (Mashayek et al., 2024), seamounts are implicitly smoothed by the inherent resolution of regional models and often further (explicitly) smoothed to avoid errors in sigma-coordinate models (Mellor et al., 1998; Sikirić et al., 2009). However, investigations from the atmospheric science community suggest that small-scale features on mountains play a crucial role in modulating energy dissipation and flow dynamics, with implications that should parallel those found in oceanic systems. In atmospheric flows over complex terrain, unresolved subgrid-scale topography generates significant drag forces and dissipation that often need to be parameterized in global circulation models (Lott & Miller, 1997; Scinocca & McFarlane, 2000). Furthermore, small-scale details of mountains have been shown to change dynamics in both numerical and observational experiments (Aebischer & Schär, 1998; Schär, 2002; Schär et al., 2003), suggesting similar effects may likewise occur for seamounts. Indeed, recent work has indicated that parameterized turbulent mixing is increased in hydrostatic simulations of a seamount that partially resolve the fine-scale topographic variability (Aghor et al., 2026). Since our ability to represent these high dissipation rates is fundamentally limited by resolution constraints, especially in global and regional ocean models, the impacts of seamount (and, more generally, topographic) roughness should be well-understood, so that they can be taken into account when appropriate.

In this paper we use Large-Eddy Simulations (LES) to show that resolved roughness can significantly modify seamount wake energetics, often leading to differences larger than an order of magnitude. We focus our detailed analysis on the case of weakly stratified, rotating seamounts in Section 3 (since they are the most affected by small-scale roughness), where we show that small-scale bathymetric variation can increase kinetic energy (KE) dissipation by an order of magnitude, while increasing mixing by a factor of three. We also run a general parameter sweep in Section 4, and use results to investigate implications for global energetics in Section 5. Specifically, because the seamounts whose energetics are impacted by roughness are concentrated in the energetic flows of the Southern Ocean, we estimate that up to 30% of the total dissipation by seamounts globally may be attributed to small-scale bathymetric variability.

2. Computational Model and Simulations

We use turbulence-resolving Large-Eddy Simulations (LES) implemented using the Julia package Oceananigans (Ramadhan et al., 2020; Wagner et al., 2025) for all simulations in this work. The simulations solve the filtered nonhydrostatic incompressible Boussinesq equations with subgrid-scale turbulence modeled using a Lagrangian-averaged dynamic Smagorinsky closure (Bou-Zeid et al., 2005). The domain is periodic in the meridional direction with inflow-outflow conditions in the zonal direction and an immersed boundary method to represent the bathymetry. Complete details on the numerical implementation, boundary conditions, and discretization—including specific schemes, pressure treatment, SGS closure, and grid structure—are provided in Section S1 of Supporting Information S1 (Adcroft et al., 1997; Bou-Zeid et al., 2005; Chamecki et al., 2019; Kleissl et al., 2006; Ramadhan et al., 2020; Wagner et al., 2025) and some key quantities can be found in Table 1.

At the origin of our coordinate system there is a seamount whose bathymetric data was taken from the Balanus seamount (of the New England seamounts) using the Global Multi-Resolution Topography Synthesis (Ryan et al., 2009). Balanus was chosen because it is very well-surveyed and has an approximately Gaussian shape, facilitating comparisons with other idealized studies. Note that, in order to generalize the horizontal scale to non-idealized seamounts, we use the Full Width at Half Maximum (FWHM) as the relevant horizontal width W (calculated here as the square root of the seamount area at half its height).

Given the constraints of LES (which needs to have $\mathcal{O}(1)$ m resolution in the ocean), the seamount was scaled down to fit into a computationally-feasible domain size, while preserving realistic values of nondimensional parameters. While this approach is standard in the literature and is equivalent to running a dimensionless simulation (Liu et al., 2024; Puthan et al., 2022), which conserves dynamics in high enough Reynolds number flows (Chor & Wenegrat, 2025; Jalali & Sarkar, 2017). One requirement for dynamical similarity in our case is that the (attached) bottom boundary layer thickness needs to be much smaller than the size of the obstacle, which

Table 1
Parameters Used by Simulations in the Present Work Along With Their Definitions and Values

Parameter	Definition	Value
Lx	Domain length (zonal)	3,500 m
Ly	Domain length (meridional)	2,000 m
Lz	Domain height (vertical)	200 m
$\Delta x, \Delta y$	Horizontal grid spacing	2 m
Δz	Vertical grid spacing for $z \in [0, H]$	1 m
U_∞	Background velocity	0.1 m s^{-1}
N_∞	Background stratification	$[5, 10, 33, 125, 250] \times 10^{-4}$ s^{-1}
f	Coriolis frequency	$[-4, -10, -20, -40] \times 10^{-4}$ s^{-1}
L	Smoothing scale	[0, 0.05, 0.1, 0.4, 0.8] W
W (FWHM)	Seamount width (Full Width at Half Maximum)	500 m
H	Seamount height	100 m
Ro_b	Bathymetric Rossby number ($U_\infty/\lvert f\rvert W$)	[0.05, 0.1, 0.2, 0.5]
Fr_b	Bathymetric Froude number ($U_\infty/N_\infty H$)	[0.04, 0.08, 0.3, 1, 2]
S_b	Slope Burger number ($Ro_b/Fr_b = N_\infty H/\lvert f\rvert W$)	(varies by combining Ro_b and Fr_b above)

Note. The smoothing scale L refers to the resolution at which bathymetry is coarsened before interpolation back to the high-resolution grid (in order to smooth it). Note also that Mashayek et al. (2024) define their Burger number as the square of S_b. Finally, note that the high values of f and N_∞ are necessary to achieve realistic values of the dynamically-relevant nondimensional parameters (see discussion about dynamical similarity in Section 2).

is observed. To make implications more intuitive, we occasionally scale up our results to match typical seamount dimensions when presenting key results—typically FWHM $= W = 10$ km (Kim & Wessel, 2011). We indicate when this occurs; otherwise, results use the simulation dimensions.

Note also that we can rescale the seamount independently in the vertical and horizontal directions, giving us control of the aspect ratio $\delta = H/W$. This allowed us to try simulations using Balanus with different aspect ratios, where we verified that δ has only a small impact on wake energetics of simulations for ocean-relevant values. Instead the main dynamical consequence of a higher δ, is that it limits the permitted range of lee waves, which are only allowed when $|f| < U_\infty k < N_\infty = S_b|f|/\delta$, where k is a horizontal perturbation wavenumber, dictated in our case by the seamount (Baker & Mashayek, 2022). Thus, no lee waves are allowed when $\delta \geq S_b$. Given that both previous studies (Aravind et al., 2026) and preliminary investigations indicate that the presence of waves does not significantly modify energetics (see Section S2 in Supporting Information S1), we use $\delta = 0.2$ in our simulations, excluding lee waves. Finally, simulations were run where the flow impinges on the seamount at different angles, with no appreciable differences observed in the results, suggesting that the effects discussed here are likely independent of specific bathymetric features.

The bottom geometry is depicted in the top row of Figure 1, with the original seamount shown in the left panel and a smoothed version (with a smoothing scale $L = 0.8W$) shown in the right panel. The smoothing, whose purpose is discussed in Sections 3 and 4, was performed by coarsening the original bathymetry data to a given resolution (named the smoothing scale L) and interpolating it back into the original high-resolution grid, which mimics the smoothed geometries used in idealized studies, and missing subgrid-scale variance inherent in larger-scale realistic modeling.

3. Low-S_b Seamounts (Representative of the Southern Ocean)

We start our analysis focusing on seamounts that have a moderately low Slope Burger number S_b. As will be shown in Section 4, the energetics of seamounts in this regime are highly sensitive to roughness. Furthermore, taking data from Mashayek et al. (2024) as a basis, we see these seamounts are common in the Southern Ocean, which experiences especially energetic flows. Given that the total contribution to dissipation by an individual seamount can be estimated as

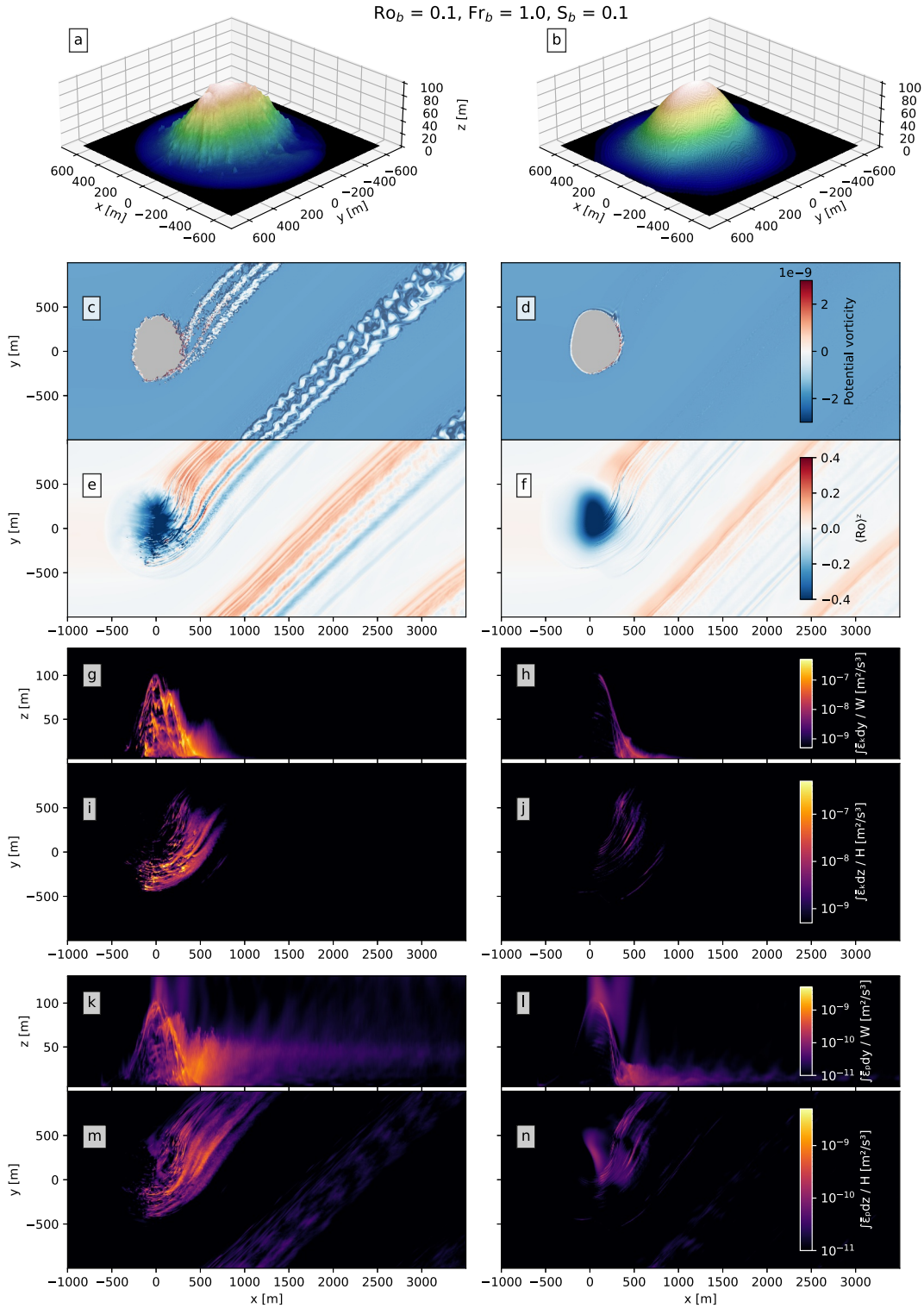

Figure 1. Left column shows results for the a rough seamount ($L = 0$) and right column shows results for a smooth one ($L = 0.8W$). Top row: bathymetry used in the simulations. Second row: instantaneous snapshots of horizontal cross-sections of Ertel PV at $z = H/3$ (note that the background PV is negative since $f < 0$). Third row: time- and vertically-averaged pointwise Rossby number (vertical vorticity $/f$); note the vertically coherent anticyclone on top of the topography, visible as a patch of negative Rossby number. Fourth row: time-averaged, cross-direction-integrated KE dissipation rates. Fifth row: time-averaged, vertically-integrated KE dissipation rates. Sixth row: time-averaged, cross-direction-integrated buoyancy mixing rates. Seventh row: time-averaged, vertically-integrated buoyancy mixing rates.

$$\iiint \varepsilon_k dx\, dy\, dz \propto U_\infty^3 W^2, \tag{1}$$

we expect such a regime to be particularly important for global energetics given the cubic dependence on velocity (see also Section 5 for a quantitative assessment).

We simulate a seamount interaction with $Ro_b = 0.1$, $Fr_b = 1$ (achieved with $N_\infty = 1.25 \times 10^{-3}$ s^{-1} and $f = -2 \times 10^{-3}$ s^{-1}, leading to $S_b = 0.1$) in a deep water region where $U_\infty \approx 0.1$ m/s (Mashayek et al., 2024; Figure 1; Figures S1 and S2 in Supporting Information S1). We run these simulations with six different levels of smoothing, given by values of smoothing scale $L = (0, 0.05, 0.1, 0.2, 0.4, 0.8)W$ (the smoothing procedure is explained in the last paragraph of Section 2). Note that, while this set-up does not allow lee waves (since $S_b/\delta < 1$), we verified that a similar set-up which does support them produces similar results (see Section 2 in Supporting Information S1).

3.1. General Dynamics

In all simulations in this section, once the initial adjustment period passes, the larger scales of the wake are largely time-independent, with the only visible time variability being due to small-scale turbulence. While the amount of turbulence is a function of the resolved roughness, the seamount-scale dynamics approximately follow the solution by Hogg (1973)'s "weak stratification" regime. Namely, the largest feature of the flow is a single, isolated, vertically-coherent anticyclone at the top of the seamount—also in accordance with Perfect et al. (2018)'s regime expectations. This feature can be seen in Figures 1e and 1f (which shows a vertical average of the vertical vorticity normalized by f) for rough and smooth seamounts, respectively. Even for the rough seamount, this anticyclone is dominant, with the main difference being its close-following of rough topographic contours compared to the smooth version.

Differently from the idealized solution, but similar to previous investigations Srinivasan et al., 2019, first simulation in their Table 1), our simulations exhibit a weak, mostly-cyclonic wake, likely resulting from bottom drag (Srinivasan et al., 2019). Note that this wake detaches on the cyclonic side of the seamount and a mean cross-stream velocity also develops toward the same side. This feature can be seen in previous works with weakly stratified, rotating environments (Jagannathan et al., 2021; Perfect et al., 2020b; Srinivasan et al., 2019) and one possible interpretation relates to the breaking of geostrophic balance in the vicinity of the seamount. This causes the geostrophic pressure gradient included in the North-South direction (see Equation 1 in Supporting Information S1) to become momentarily unbalanced, creating a net cross-stream acceleration. We observed that, for long enough domains in the x direction, geostrophic balance is regained sufficiently far downstream, leading the flow to realign in the East-West direction. While we do not show these longer-domain simulations here, this realignment can be seen clearly in Figure 1 of Srinivasan et al. (2019).

Importantly, the wake has larger values of Ro for the rough seamount, most apparent as streaks of anticyclonic vorticity, which are a product of the smaller horizontal scales present in the rough bathymetry. These higher values of vorticity imprint on the Ertel potential vorticity ($\mathrm{PV} = \vec{\nabla} b \cdot \left[\vec{\nabla} \times \vec{u} + f\vec{k}\right]$), a horizontal-cross section of which is shown in Figures 1c and 1d. Such an imprint (likely originating due to flow splitting at the small scales Schär et al., 2003) leads to streaks in PV that emanate from the rough seamount which have been reported in the atmospheric literature, where they are known as "PV banners" (Schär, 2002; Schär et al., 2003). These banners—absent from the smooth bathymetry—have been observed experimentally in atmospheric flows (Schär et al., 2003) and are known to affect flow dynamics downstream. Interestingly, while PV banners are often observed to have alternating positive-negative PV signals, in this case we see alternating positive-zero signals. This is likely due to turbulent mixing (either due to centrifugal instabilities or 3D turbulence from the seamount boundary layer) entraining high-PV ambient water, thus bringing negative-PV regions back to zero (Chor & Wenegrat, 2025; Haine & Marshall, 1998; Srinivasan et al., 2021).

3.2. Turbulence and Energetics

While the large-scale dynamics of the solutions are similar between rough and smooth seamounts, the energetics are distinct. Figures 1g–1j shows vertical and horizontal profiles of KE dissipation rate for both seamounts, and it is clear that the rough bathymetry is significantly more dissipative than the smooth one. Furthermore, patches of

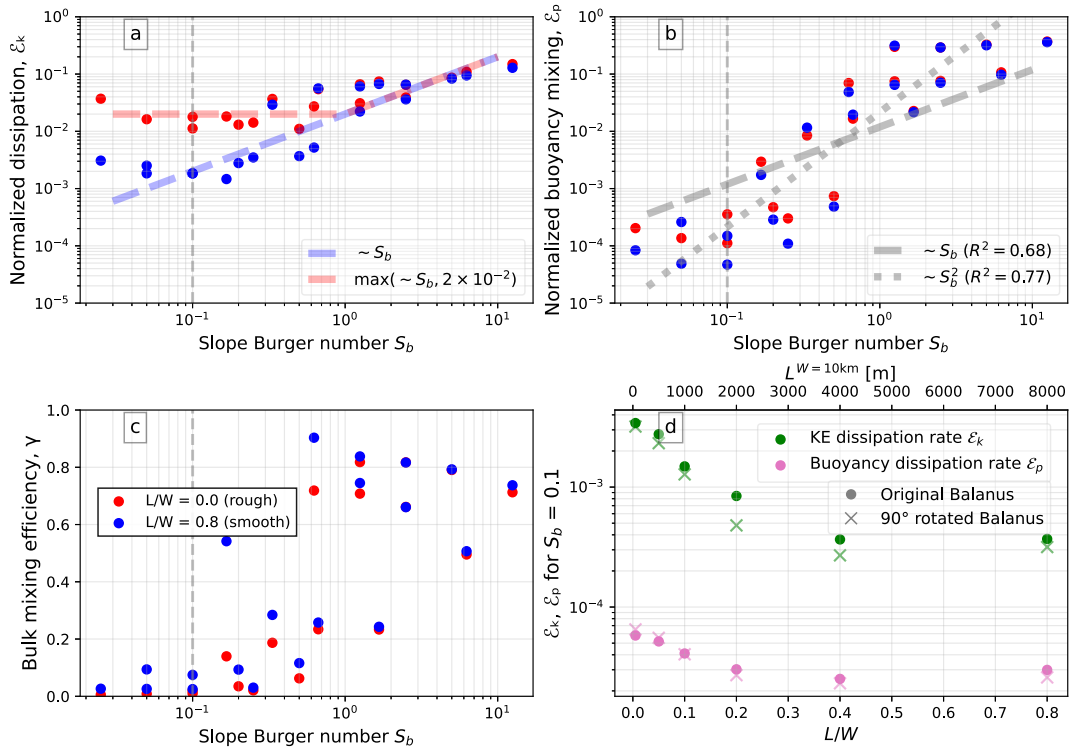

Figure 2. Normalized KE dissipation (panel a), buoyancy mixing (panel b), and mixing efficiency (panel c) as a function of the bathymetric Slope Burger number S_b. Red points are results from simulations with rough bathymetry (smoothing length scale $L = 0$) and blue points are results from smooth bathymetry (smoothed with a length scale $L = 0.8W$). Dashed and dotted lines are present as references, with their scaling shown in the legend. Panel d shows normalized time- and volume-averaged KE dissipation (green) and buoyancy mixing (magenta) as a function of L/W for a seamount with $Ro_b = 0.1$, $Fr_b = 1$ and $S_b = 0.1$. Circles show results for an un-rotated seamount, while crosses show results for 90°-rotated seamount. The top axis in panel d shows the smoothing scale for a typical ocean seamount of $W = 10$ km, $L^{10\text{km}}$. Note that for panel d we consider the un-smoothed bathymetry to have a scale of the grid's horizontal spacing, which equals $L/W = 0.005$ or $L^{W=10\text{km}} = 50$ m. Vertical gray dashed lines in panels a, b, and c indicate the parameter regime for results in panel d ($S_b = 0.1$).

high dissipation (in both cases) are co-located with regions of large-magnitude small-scale vorticity (compare with Figures 1e and 1f)—a consequence of horizontal shear having a leading role in creating turbulence (see Section S3 in Supporting Information S1).

Moreover, while the peak of KE dissipation ε_k happens very close to the seamount and is more clearly impacted by the small-scale roughness, large values of buoyancy mixing ε_p tend to be more spread out along the wake. This effect can be seen more clearly when comparing Figures 2g and 2i with Figures 2k and 2m. Also interesting is the fact that mixing happens higher in the water column for the rough case (being concentrated at $z \approx H/2$) than for the smooth case, where it is mostly concentrated at the bottom, which can be seen when comparing panels k and l of the same figure. A similar effect can be seen for the KE dissipation, although not as striking. We attribute this effect to the small-scale bathymetry prompting a more efficient wake separation, with the flow remaining approximately attached in the smooth seamount.

In order to get a better assessment of the turbulence dependence on smoothness/roughness, we plot the normalized, time- and volume-averaged KE dissipation in Figure 2d as a function of the normalized smoothing scale L/W as green circles. It is clear that there is a monotonic trend to lower dissipation rates as the bathymetry becomes smoother, with a steep initial drop (≈50%) already happening for $L/W = 0.1$. This difference stabilizes at around an order of magnitude for $L/W \approx 0.4$, and further smoothing does not further decrease dissipation. Similar results are shown for mixing as magenta circles in the same panel. Although quantitatively not as dramatic as results for dissipation, smoothing still accounts for a roughly 3-fold difference in buoyancy mixing. These results are independent of seamount orientation, which can be seen in Figure 2d where crosses indicate cases run with the bathymetry rotated by 90°. Finally, the top horizontal axis of Figure 2d shows what the smoothing scale

would be for a typical seamount of $W = 10$ km (i.e., $L^{W=10\text{km}}$, where we scale up all dimensions by a factor of 10 km/500 m = 20), revealing that dissipation and mixing are already at a minimum with $L^{W=10\text{km}} = 4$ km. Figure 2d also suggests that resolving bathymetric details on the order of $L^{W=10\text{km}} = 50$ m (corresponding approximately our numerical resolution of 2 m multiplied by the scaling factor of 20) may be necessary to capture the full effects of mixing and dissipation.

4. Parameter Sweep

We now examine how roughness influences bulk energetics across various regions of the parameter space, characterized here by Ro_b and Fr_b. Globally, Ro_b for seamounts typically falls within 0.05–0.5, while Fr_b is more broadly distributed, generally between 0.04 and 2 (based on data by Mashayek et al. [2024]). Accordingly, we perform 20 simulations covering Ro_b and Fr_b values listed in Table 1, achieved by varying f and N_∞. We estimate the normalized, time-averaged, volume-integrated KE dissipation and buoyancy mixing rates resulting from flow-seamount interactions as

$$\mathcal{E}_k = \frac{\iiint \overline{\varepsilon}_k dx\, dy\, dz}{U_\infty^3 W^2}, \tag{2}$$

$$\mathcal{E}_p = \frac{\iiint \overline{\varepsilon}_p dx\, dy\, dz}{U_\infty^3 W^2}, \tag{3}$$

where $\overline{(\cdot)}$ is a time-averaging operation, and the normalization comes from assuming $\iiint (\cdot) dx\, dy\, dz \sim L^2 H$ and $\varepsilon_k \sim U_\infty^3/H$—which has been numerically verified. Note that this scaling is slightly different than the one used by Chor and Wenegrat (2025) (who assumed $\varepsilon_k \sim U_\infty^3/L$), since there is some ambiguity in the definition of the length scale in this case, mostly due to possible changes in the physics with varying $\delta = H/W$.

Figure 2a shows results for $\mathcal{E}_k$ as a function of the bathymetric Slope Burger number S_b. Consistent with Chor and Wenegrat (2025), dissipation rates are reasonably well organized by S_b. This contrasts with results by Liu et al. (2025), which found that the dependence of dissipation on Fr_b and Ro_b cannot be expressed by a single parameter. In particular, they found that the effect of Ro_b can be non-monotonic for moderate stratifications, which could be attributed to differences in seamount geometry (namely, aspect ratio and seamount shape). Importantly, while it is clear that $\mathcal{E}_k$ results are organized by S_b, Figure 2a points to a significant difference between $\mathcal{E}_k$ generated by rough seamounts in comparison to smooth ones. Namely, for medium to large values of S_b, $\mathcal{E}_k$ scales approximately linearly with Slope Burger number, similar to results observed by Chor and Wenegrat (2025) for a headland. However, for low values of S_b, normalized dissipation rates asymptote to a constant value of $\mathcal{O}(10^{-2})$ when using the full resolution topography. Therefore Figure 2a suggests that the largest relative contribution of small-scale roughness to energetics happens for flows with low Slope Burger numbers. Specifically, differences between rough and smooth seamount dissipations in Figure 2a for $S_b \approx 0.1$ are of an order of magnitude, consistent with the results of Section 3.

Note that a constant-value asymptote for low Slope Burger numbers is not unexpected given that S_b measures the dynamic steepness of the seamount. In particular, as S_b decreases, the seamount becomes dynamically flatter, and its effects on the flow accordingly become smaller. This continues until the S_b is small enough that the effects of the larger scales of the seamount become smaller than the effects of the seamount roughness. At this point further decreasing the value of S_b does not further reduce the dissipation since $\mathcal{E}_k$ is dominated by roughness effects. Hence, the value of both the S_b at which transition happens and the baseline dissipation for the asymptote likely depends on the obstacle's roughness (either resolved or parameterized). Accordingly, we would also expect the smooth seamount to reach an asymptote at small enough S_b values, albeit at a much smaller dissipation value.

Results for $\mathcal{E}_p$ are shown in Figure 2b, where an organization with S_b is also clear and, importantly, there is a smaller difference between buoyancy mixing in rough and smooth seamounts. Again consistent with Section 3 results, these differences can reach a factor of three, and are also more prominent in low-S_b seamounts. Furthermore, in contrast to $\mathcal{E}_k$, our results show that $\mathcal{E}_p$ scales slightly better with S_b^2 than with S_b, with coefficients of determination of $R^2 = 0.77$ and 0.68, respectively. While not definitive, the better fit for S_b^2 differs from the

linear dependence on S_b found by Chor and Wenegrat (2025), suggesting a possible dependence on geometry for $\mathcal{E}_p$

This quadratic scaling for $\mathcal{E}_p$, coupled with the linear scaling for $\mathcal{E}_k$ further implies a change in mixing efficiency ($\gamma = \mathcal{E}_p/(\mathcal{E}_p + \mathcal{E}_k)$) with Slope Burger number, shown in Figure 2c. Results reveal near-zero γ values for low Slope Burger numbers, with mixing efficiency values increasing with increasing S_b. Mixing efficiency then saturates at $\gamma \approx 0.8$ for Slope Burger number of unity and higher, which is when the vertical decoupling effect of stratification surpasses the organization effects of rotation. Given that high Slope Burger seamounts tend to be concentrated close to the Equator (Mashayek et al., 2024; Figure 1e), this implies that low-latitude seamounts may tend to be particularly efficient in mixing buoyancy, although that is not pursued further here (see Section S4 in Supporting Information S1). We note that such high values of γ are usually seen in cases where gravitational instabilities produce turbulence (Chalamalla & Sarkar, 2015; Wykes & Dalziel, 2014), which is not expected in our case given the weak stratification and subsequent dominance of shear production (see Section S3 in Supporting Information S1). While the mixing efficiency depends on many aspects of the flow (Caulfield, 2021) and while dynamic Smagorinsky closures have been shown to produce accurate estimates of mixing efficiency (Chalamalla & Sarkar, 2015), this result should be interpreted with caution, and validation with different methods (such as laboratory experiments or direct numerical simulations) is recommended, but left for future work.

Finally, while results in this section imply a strong dependence of seamount energetics on S_b, evidence suggests that this is not the case for dynamical features of the flow. As mentioned, Chor and Wenegrat (2025) found a similar dependence on S_b for headland energetics, but showed that dynamics vary widely with both Rossby and Froude numbers in ways that cannot be captured solely by the Slope Burger number. We found similar results here for the dynamics of both rough and smooth seamounts (not shown), and a similar conclusion was reached by Liu et al. (2024, Section 3) when analyzing wake vortex shedding frequency and comparing it to Burger-number-based predictions by Perfect et al. (2018).

5. Implications for Global Energetics

Results in Sections 3 and 4 reveal significant differences between rough and smooth seamounts. In particular, given the difference in scaling between both cases in Figure 2a, we are prompted to explore large-scale implications for both configurations. We begin by approximating the dissipation around both rough and smooth seamounts separately according to

$$\mathcal{E}_k^{\text{smooth}} = 2 \times 10^{-2} S_b, \tag{4}$$

$$\mathcal{E}_k^{\text{rough}} = \max\left(\mathcal{E}_k^{\text{smooth}}, 2 \times 10^{-2}\right). \tag{5}$$

Both curves are shown in Figure 2a as dashed lines. (The curves described by Equations 4 and 5 were verified to have R^2 values ranging between approximately 0.5 and 0.75. Note that, rather than using lines of best fit, we enforce that the curves for rough and smooth seamounts match for large S_b values since we physically expect that to be the case. See the discussion about this topic in Section 4.) We can use Equations 2–5, to estimate the integrated dissipation by each mapped seamount individually using data made available by Mashayek et al. (2024), giving us global estimates of seamount contributions to dissipation and mixing.

Dissipation results are shown in Figures 3a and 3b for smooth and rough seamounts, respectively. It is clear that most of the seamount-led dissipation happens in the Southern Ocean regardless of seamount roughness, as expected due to the cubic velocity dependence in Equation 1. That said, dissipation rates are clearly higher for rough seamounts, evident in Figure 3c, which shows zonally-integrated dissipation for both cases. These results suggest that seamount roughness (i.e., small-scale bathymetric variability) may account for approximately 30% of the seamount contribution to KE dissipation in the global ocean, and 40% in the Southern Ocean specifically.

Moreover, these results suggest that small-scale topographic features, while perhaps secondary for local dynamics, can change the energetics significantly. Taking the dimensions of our geometry and scaling them up to representative Southern Ocean seamount sizes (≈10 km FWHM; see Figure 2d), our results imply that, by not representing bathymetric details smaller than 500 m, a model could underestimate dissipation rates by 30%–50%

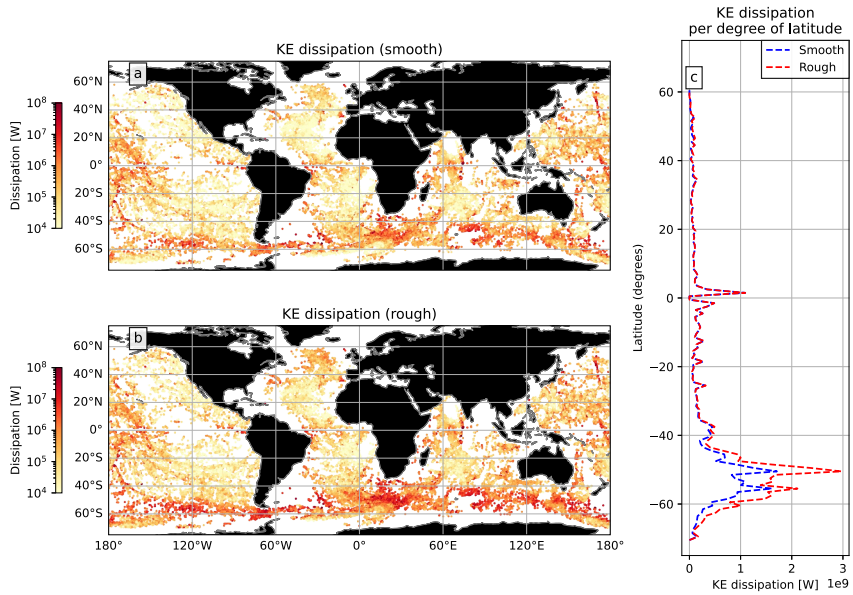

Figure 3. Global integrated seamount dissipation (panels a, b) and mixing (panels d, e). Panel a shows KE dissipation using the scaling for smooth seamounts, while panel b shows the same results using the model for rough seamounts. Panel d shows buoyancy mixing using a linear dependence on S_b, while panel (e) shows the same results but assuming a quadratic dependence. Panels (c and f) show zonally-integrated dissipation and buoyancy per degree of latitude.

around a given Southern Ocean seamount. This further implies that horizontal grid spacings of ≈100 m or smaller are necessary to capture representative seamount energetics in the south.

Beyond the resolution of the topography itself, there may be additional problems with model representation of the forward energy cascade. Although turbulence closures in regional ocean models are generally designed to capture energy production associated with vertical shear, our simulations show that horizontal shear production also plays a significant role (see Section S3 in Supporting Information S1). However, horizontal shear production is not accounted for in most commonly-used turbulence closure schemes. As a result, present parameterizations have limited ability to represent the full range of energetics associated with rough seamounts, such that even regional simulations with resolved topography may not appropriately represent wake mixing (cf. Aghor et al. (2026)).

To address this gap, turbulence closures could be expanded in one of two ways: by explicitly including the effects of horizontal shear production, or by parametrizing the impact of unresolved small-scale topography—much like existing wave drag parameterizations (Baker & Mashayek, 2022; Jayne & St. Laurent, 2001; Kim et al., 2003; Scinocca & McFarlane, 2000), some of which incorporate statistical representations of subgrid-scale topography (Lott & Miller, 1997). Implementing these improvements will also require more comprehensive high-resolution bathymetric data to accurately describe sub-grid scale variability, which is presently limited.

6. Conclusions

Understanding the energetic impact of seamounts on ocean turbulence and mixing is essential both for our understanding of global dynamics and for accurately representing oceanographic processes in numerical models. Despite the important role played by seamounts as prominent drivers of turbulent dissipation and mixing, the effect of small-scale bathymetric roughness on their energetics had not been systematically studied. With this in mind, we used turbulence-resolving nonhydrostatic large-eddy simulations to systematically explore the difference in energetics between rough and smooth seamounts.

Our findings indicate that small-scale bathymetric roughness substantially enhances dissipation and mixing in comparison to smooth seamounts. These differences are especially evident for seamounts with low Slope Burger numbers $\left(S_b \lessapprox 1\right)$, where kinetic energy dissipation can be up to an order of magnitude higher in rough cases, and buoyancy mixing rates are roughly three times larger. These seamounts are primarily found in the Southern Ocean, a region where strong currents make them particularly influential in the global energy budget (see

Equation 1). Our results further indicate that omitting roughness can lead to an underestimation of global ocean dissipation by approximately 30%, indicating a leading-order effect of small-scale topographic features. Accurately resolving these effects would require grid resolutions finer than 100 m, which is not yet practical for global simulations. Consequently, it is essential that current models and their parameterizations properly represent the influence of unresolved roughness and turbulence (see discussion in Section 5).

While the main simulations in this work do not allow lee waves, their role was investigated and found to not significantly alter energetics (Section S2 in Supporting Information S1; Aravind et al., 2026). With that said, for a sufficiently large gap between f and N_∞, roughness may also impact the production of wave energy since small-scale waves would be permitted. Given that the smallest possible waves usually have length scales of ≈600 m in the Southern Ocean (Baker & Mashayek, 2022) (corresponding to $L/W \approx 0.05$ for a typical seamount size of $W = 10$ km), investigating this topic would have required prohibitively large simulations in our configurations, and likely requires different methods of investigation. Finally, although not shown here, preliminary investigations suggest that the effect of roughness may be more pronounced (and relevant over larger parts of the parameter space) in shallow-water environments—an effect we leave for future studies. We consider both these issues, as well as investigations into possible parameterizations for the effects discussed in this manuscript, to be important future work with potentially global implications.

Conflict of Interest

The authors declare no conflicts of interest relevant to this study.

Availability Statement

The numerical model simulations upon which this study is based are too large to easily archive or transfer. Instead, all the code used to generate the results is available at https://doi.org/10.5281/zenodo.19633093 (Chor, 2025).

Acknowledgments
T. C. and J. O. W. were supported by the National Science Foundation Grant OCE-2242182 (T. C. and J. O. W.), and Office of Naval Research Grant N000142412583 (J. O. W.) GLW's work was supported by Schmidt Sciences, LLC and by the National Science Foundation Grant AGS-183557. We would also like to acknowledge high-performance computing support from Casper (https://doi.org/10.5065/qx9a-pg09) provided by NCAR's Computational and Information Systems Laboratory, sponsored by the National Science Foundation.

References

Adcroft, A., Hill, C., & Marshall, J. (1997). Representation of topography by shaved cells in a height coordinate ocean model. *Monthly Weather Review*, *125*(9), 2293–2315. https://doi.org/10.1175/1520-0493(1997)125⟨2293:ROTBSC⟩2.0.CO;2

Aebischer, U., & Schär, C. (1998). Low-level potential vorticity and cyclogenesis to the lee of the alps. *Journal of the Atmospheric Sciences*, *55*(2), 186–207. https://doi.org/10.1175/1520-0469(1998)055⟨0186:LLPVAC⟩2.0.CO;2

Aghor, P. P., McKinley, M., & Bracco, A. (2026). Interaction of ocean currents and seamounts: Near-bottom dynamics around atlantis ii. *Journal of Geophysical Research: Oceans*, *131*(3), e2025JC023167. https://doi.org/10.1029/2025JC023167

Aravind, H. M., Puthan, P., Sarkar, S., Merrifield, S., & Terrill, E. (2026). Tidally dominated flows past a three-dimensional topography: Wake vortices, turbulence, and mixing. *Journal of Physical Oceanography*, *56*(2), 371–390. https://doi.org/10.1175/JPO-D-25-0108.1

Baker, L. E., & Mashayek, A. (2022). The impact of representations of realistic topography on parameterized oceanic lee wave energy flux. *Journal of Geophysical Research: Oceans*, *127*(10), e2022JC018995. https://doi.org/10.1029/2022JC018995

Bou-Zeid, E., Meneveau, C., & Parlange, M. (2005). 01). A scale-dependent lagrangian dynamic model for large eddy simulation of complex turbulent flows. *Physics of Fluids*, *17*(2), 025105. https://doi.org/10.1063/1.1839152

Caulfield, C. (2021). Layering, instabilities, and mixing in turbulent stratified flows. *Annual Review of Fluid Mechanics*, *53*(1), 113–145. https://doi.org/10.1146/annurev-fluid-042320-100458

Chalamalla, V. K., & Sarkar, S. (2015). Mixing, dissipation rate, and their overturn-based estimates in a near-bottom turbulent flow driven by internal tides. *Journal of Physical Oceanography*, *45*(8), 1969–1987. https://doi.org/10.1175/JPO-D-14-0057.1

Chamecki, M., Chor, T., Yang, D., & Meneveau, C. (2019). Material transport in the ocean mixed layer: Recent developments enabled by large eddy simulations. *Reviews of Geophysics*, *57*(4), 1338–1371. https://doi.org/10.1029/2019rg000655

Chor, T. (2025). Code for the paper "Turbulent mixing and dissipation around rough seamounts" [Software]. *Zenodo*. https://doi.org/10.5281/zenodo.19633093

Chor, T., & Wenegrat, J. O. (2025). The turbulent dynamics of anticyclonic submesoscale headland wakes. *Journal of Physical Oceanography*, *55*(6), 737–759. https://doi.org/10.1175/JPO-D-24-0139.1

Gula, J., Molemaker, M. J., & McWilliams, J. C. (2016). Topographic generation of submesoscale centrifugal instability and energy dissipation. *Nature Communications*, *7*(1), 1–7. https://doi.org/10.1038/ncomms12811

Haine, T. W., & Marshall, J. (1998). Gravitational, symmetric, and baroclinic instability of the ocean mixed layer. *Journal of Physical Oceanography*, *28*(4), 634–658. https://doi.org/10.1175/1520-0485(1998)028<0634:gsabio>2.0.co;2

Hogg, N. G. (1973). On the stratified taylor column. *Journal of Fluid Mechanics*, *58*(3), 517–537. https://doi.org/10.1017/S0022112073002302

Jagannathan, A., Srinivasan, K., McWilliams, J. C., Molemaker, M. J., & Stewart, A. L. (2021). Boundary-layer-mediated vorticity generation in currents over sloping bathymetry. *Journal of Physical Oceanography*, *51*(6), 1757–1778. https://doi.org/10.1175/JPO-D-20-0253.1

Jalali, M., & Sarkar, S. (2017). Large eddy simulation of flow and turbulence at the steep topography of luzon strait. *Geophysical Research Letters*, *44*(18), 9440–9448. https://doi.org/10.1002/2017GL074119

Jayne, S. R., & St. Laurent, L. C. (2001). Parameterizing tidal dissipation over rough topography. *Geophysical Research Letters*, *28*(5), 811–814. https://doi.org/10.1029/2000GL012044

Kim, S., & Wessel, P. (2011). New global seamount census from altimetry-derived gravity data. *Geophysical Journal International*, *186*(2), 615–631. https://doi.org/10.1111/j.1365-246X.2011.05076.x

Kim, Y., Eckermann, S. D., & Chun, H. (2003). An overview of the past, present and future of gravity-wave drag parametrization for numerical climate and weather prediction models. *Atmosphere-Ocean*, *41*(1), 65–98. https://doi.org/10.3137/ao.410105

Kleissl, J., Kumar, V., Meneveau, C., & Parlange, M. B. (2006). Numerical study of dynamic smagorinsky models in large-eddy simulation of the atmospheric boundary layer: Validation in stable and unstable conditions. *Water Resources Research*, *42*(6). https://doi.org/10.1029/2005WR004685

Liu, J., Puthan, P., & Sarkar, S. (2024). Effect of rotation on wake vortices in stratified flow. *Journal of Fluid Mechanics*, *999*, A44. https://doi.org/10.1017/jfm.2024.721

Liu, J., Puthan, P., & Sarkar, S. (2025). Turbulence in stratified rotating topographic wakes. *Journal of Physical Oceanography*, *55*(11), 2159–2177. https://doi.org/10.1175/JPO-D-25-0035.1

Lott, F., & Miller, M. J. (1997). A new subgrid-scale orographic drag parametrization: Its formulation and testing. *Quarterly Journal of the Royal Meteorological Society*, *123*(537), 101–127. https://doi.org/10.1002/qj.49712353704

Mashayek, A., Gula, J., Baker, L. E., Naveira Garabato, A. C., Cimoli, L., Riley, J. J., & de Lavergne, C. (2024). On the role of seamounts in upwelling deep-ocean waters through turbulent mixing. *Proceedings of the National Academy of Sciences*, *121*(27), e2322163121. https://doi.org/10.1073/pnas.2322163121

Mellor, G. L., Oey, L.-Y., & Ezer, T. (1998). Sigma coordinate pressure gradient errors and the seamount problem. *Journal of Atmospheric and Oceanic Technology*, *15*(5), 1122–1131. https://doi.org/10.1175/1520-0426(1998)015⟨1122:SCPGEA⟩2.0.CO;2

Munk, W., & Wunsch, C. (1998). Abyssal recipes ii: Energetics of tidal and wind mixing. *Deep Sea Research Part I: Oceanographic Research Papers*, *45*(12), 1977–2010. https://doi.org/10.1016/s0967-0637(98)00070-3

Nagai, T., Hasegawa, D., Tsutsumi, E., Nakamura, H., Nishina, A., Senjyu, T., et al. (2021). The kuroshio flowing over seamounts and associated submesoscale flows drive 100-km-wide 100-1000-fold enhancement of turbulence. *Communications Earth & Environment*, *2*(1), 1–11. https://doi.org/10.1038/s43247-021-00230-7

Nikurashin, M., Ferrari, R., Grisouard, N., & Polzin, K. (2014). The impact of finite-amplitude bottom topography on internal wave generation in the southern ocean. *Journal of Physical Oceanography*, *44*(11), 2938–2950. https://doi.org/10.1175/JPO-D-13-0201.1

Perfect, B., Kumar, N., & Riley, J. (2018). Vortex structures in the wake of an idealized seamount in rotating, stratified flow. *Geophysical Research Letters*, *45*(17), 9098–9105. https://doi.org/10.1029/2018GL078703

Perfect, B., Kumar, N., & Riley, J. (2020a). Energetics of seamount wakes. Part I: Energy exchange. *Journal of Physical Oceanography*, *50*(5), 1365–1382. https://doi.org/10.1175/JPO-D-19-0105.1

Perfect, B., Kumar, N., & Riley, J. (2020b). Energetics of seamount wakes. Part II: Wave fluxes. *Journal of Physical Oceanography*, *50*(5), 1383–1398. https://doi.org/10.1175/JPO-D-19-0104.1

Puthan, P., Pawlak, G., & Sarkar, S. (2022). Wake vortices and dissipation in a tidally modulated flow past a three-dimensional topography. *Journal of Geophysical Research: Oceans*, *127*(8), e2022JC018470. https://doi.org/10.1029/2022JC018470

Ramadhan, A., Wagner, G. L., Hill, C., Campin, J.-M., Churavy, V., Besard, T., et al. (2020). Oceananigans.jl: Fast and friendly geophysical fluid dynamics on GPUs. *Journal of Open Source Software*, *5*(53), 2018. https://doi.org/10.21105/joss.02018

Ryan, W. B. F., Carbotte, S. M., Coplan, J. O., O'Hara, S., Melkonian, A., Arko, R., et al. (2009). Global multi-resolution topography synthesis. *Geochemistry, Geophysics, Geosystems*, *10*(3). https://doi.org/10.1029/2008GC002332

Schär, C. (2002). Mesoscale mountains and the larger-scale atmospheric dynamics: A review. In R. Pearce (Ed.), *Meteorology at the millennium* (Vol. 83, pp. 29–42). Academic Press. https://doi.org/10.1016/S0074-6142(02)80155-3

Schär, C., Sprenger, M., Lüthi, D., Jiang, Q., Smith, R. B., & Benoit, R. (2003). Structure and dynamics of an alpine potential-vorticity banner. *Quarterly Journal of the Royal Meteorological Society*, *129*(588), 825–855. https://doi.org/10.1256/qj.02.47

Scinocca, J. F., & McFarlane, N. A. (2000). The parametrization of drag induced by stratified flow over anisotropic orography. *Quarterly Journal of the Royal Meteorological Society*, *126*(568), 2353–2393. https://doi.org/10.1002/qj.49712656802

Sikirić, M. D., Janeković, I., & Kuzmić, M. (2009). A new approach to bathymetry smoothing in sigma-coordinate ocean models. *Ocean Modelling*, *29*(2), 128–136. https://doi.org/10.1016/j.ocemod.2009.03.009

Srinivasan, K., McWilliams, J. C., & Jagannathan, A. (2021). High vertical shear and dissipation in equatorial topographic wakes. *Journal of Physical Oceanography*, *51*(6), 1985–2001. https://doi.org/10.1175/JPO-D-20-0119.1

Srinivasan, K., McWilliams, J. C., Molemaker, M. J., & Barkan, R. (2019). Submesoscale vortical wakes in the lee of topography. *Journal of Physical Oceanography*, *49*(7), 1949–1971. https://doi.org/10.1175/JPO-D-18-0042.1

Wagner, G. L., Silvestri, S., Constantinou, N. C., Ramadhan, A., Campin, J.-M., Hill, C., et al. (2025). High-level, high-resolution ocean modeling at all scales with Oceananigans. *arXiv preprint*. https://doi.org/10.48550/arXiv.2502.14148

Waterhouse, A. F., MacKinnon, J. A., Nash, J. D., Alford, M. H., Kunze, E., Simmons, H. L., et al. (2014). Global patterns of diapycnal mixing from measurements of the turbulent dissipation rate. *Journal of Physical Oceanography*, *44*(7), 1854–1872. https://doi.org/10.1175/JPO-D-13-0104.1

Wright, C. J., Scott, R. B., Ailliot, P., & Furnival, D. (2014). Lee wave generation rates in the deep ocean. *Geophysical Research Letters*, *41*(7), 2434–2440. https://doi.org/10.1002/2013GL059087

Wykes, M. S., & Dalziel, S. B. (2014). Efficient mixing in stratified flows: Experimental study of a rayleigh–taylor unstable interface within an otherwise stable stratification. *Journal of Fluid Mechanics*, *756*, 1027–1057. https://doi.org/10.1017/jfm.2014.308